Check for updates

Numerical simulation of coupled fluid-solid interaction at the pore scale: A digital rock-physics technology

Vishal Das[1], Tapan Mukerji[2], and Gary Mavko[1]

ABSTRACT

We have used numerical modeling to capture the physics related to coupled fluid-solid interaction (FSI) and the frequency dependence of pore scale fluid flow in response to pore pressure heterogeneities at the pore scale. First, we perform numerical simulations on a simple 2D geometry consisting of a pair of connected cracks to benchmark the numerical method. We then compute and contrast the stresses and pore pressures obtained from our numerical method with the commonly used method that considers only structural mechanics, ignoring FSI. Our results demonstrate that the stresses and pore pressures of these two cases are similar for low frequencies (1 Hz). However, at higher frequencies (1 kHz), we observe pore-pressure heterogeneities from the FSI numerical method that cannot be representatively modeled using the structural mechanics approach. At even higher frequencies (100 MHz), scattering effects in the fluid give rise to higher pressure heterogeneities in the pore space. The dynamic effective P-wave modulus M, attenuation Q^{-1}, and P-wave velocity V_P were calculated using the results obtained from the numerical simulations. These results indicate a shift in the dispersion curves toward lower frequencies when the fluid viscosity is increased or when the aspect ratio of the microcrack is decreased. We then applied the numerical method on a 3D digital rock sample of Berea sandstone for a sweep of frequencies ranging from 10 Hz to 100 MHz. The calculated pore pressure at the low frequency (1 kHz) is homogeneous and the fluid is in a relaxed state, whereas at the high frequency (100 kHz), the pore pressure is heterogeneous, and the fluid is in an unrelaxed state. This type of numerical method helps in modeling and understanding the dynamic effects of fluid at different frequencies that result in velocity dispersion and attenuation.

INTRODUCTION

Digital rock physics (DRP) is becoming an indispensable tool for rock-physics analysis and reservoir characterization workflow in exploration geophysics. DRP uses high-resolution rock images obtained using micro-computed tomography (CT) scans or other imaging techniques to calculate structural, geometric, and volumetric properties of rocks (Fredrich et al., 1993; Keehm et al., 2001; Arns et al., 2005; Golab et al., 2010; Andrä et al., 2013a). Physics-based numerical simulations on the rock images are used to obtain properties such as elastic moduli, conductivity, and flow properties (Arns et al., 2001, 2002; Keehm et al., 2001; Pinczewski and Lindquist, 2001; Dvorkin et al., 2011; Madonna et al., 2012; Andrä et al., 2013b; Sain et al., 2014; Saxena and Mavko, 2016; Saxena et al., 2017a). The physical properties obtained are used in rock-physics

analysis and interpretation of data acquired using remote sensing techniques, for example, seismic data or well-log measurements. DRP technology helps to complement the measurements taken in the laboratory and models derived from empirical trends or effective medium theories. Using DRP, pore-scale details such as stress heterogeneities and the fluid velocity field can be obtained at microscale. These details are either difficult or infeasible to obtain from laboratory measurements and cannot be explained by effective medium models. DRP technology has the unique ability of setting up a virtual rock-physics laboratory that allows robust and exhaustive sets of measurements on the same digital rock sample. DRP techniques also allow us to analyze rock physics what-if extrapolation scenarios that can only be carried out using numerical computations.

The success of DRP depends on many factors, including high-resolution images of the rock, appropriate image segmentation

---

[1]Stanford University, Department of Geophysics, Stanford, California, USA. E-mail: vdas2@stanford.edu (corresponding author); gmavko@gmail.com.
[2]Stanford University, Department of Geophysics, Stanford, California, USA and Stanford University, Energy Resources Engineering Department, Stanford, California, USA. E-mail: mukerji@stanford.edu.

Table 1. Material properties corresponding to the grain and pore fluid used in the numerical simulations.

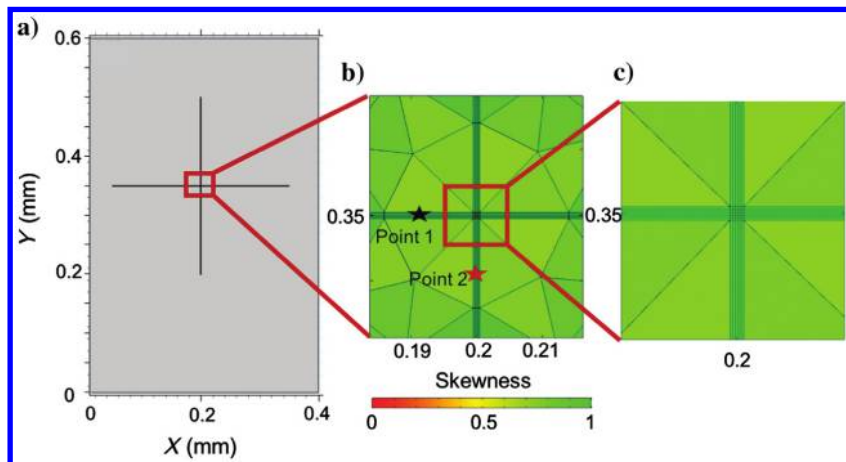| Grain		Pore fluid	
Bulk modulus (K)	36.6 GPa	Dynamic viscosity (η)	0.486 Pa-s
Shear modulus (μ)	45.5 GPa	Reference density (ρ_0) at reference pressure (P_0) = 1 atm	860 kg/m^3
Density (ρ)	2650 kg/m^3	Bulk modulus (K_f)	1.02 GPa

Figure 1. (a) The 2D connected cracks geometry with two microcracks perpendicular to each other. (b) Magnified central part of the mesh for the 2D connected cracks geometry with the skewness of the mesh elements representing the mesh quality is shown in color. Points 1 and 2 corresponding to the horizontal and vertical crack, respectively, are highlighted. The pressure at these points is analyzed. (c) A further magnified part of the mesh showing rectangular elements for the pore space and tetrahedral elements for the grain.
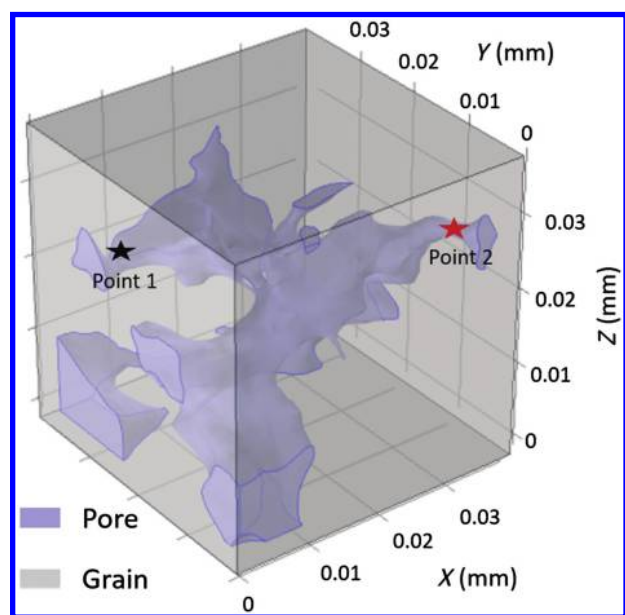

Figure 2. The 3D Berea geometry with the grain and the pore space. Points 1 and 2, corresponding to two parts of the pore space, are highlighted. The pressure at these two points is analyzed.

and meshing algorithms, proper simulation of physics, and benchmarking results obtained from simulations. The use of DRP in understanding physical phenomenon in rocks depends on the ability to simulate appropriate physics at the pore scale. The physics related to structural mechanics is often used to estimate the effective elastic properties of a digital rock sample. The calculations are done using finite-difference or finite-element methods that treat the solid grains and the fluid in the pore space as elastic material (Garboczi, 1998; Arns et al., 2002; Zhan et al., 2010; Andrä et al., 2013b; Saxena and Mavko, 2016; Saxena et al., 2017b). Assuming pore fluid to be an elastic material offers insights into the effective elastic properties under stationary conditions. This impairs the study of dynamic effects due to the presence of fluids and pore pressure induced local and global fluid flow effects. Pore fluids play a major role in velocity dispersion and attenuation on the microscopic and macroscopic scales (Mavko and Nur, 1975; O'Connell and Budiansky, 1977; Murphy et al., 1986; Mavko and Jizba, 1991; Sams et al., 1997; Chapman et al., 2002; Masson and Pride, 2007; Mavko et al., 2009; Gurevich et al., 2010; Müller et al., 2010; Quintal et al., 2011, 2016; Tisato and Quintal, 2013, 2014). These effects impact the elastic measurements obtained from seismic waves. In some recent work, dynamic effects of fluid in the pore space are modeled by assuming the Newtonian fluid as a viscoelastic material and assigning a viscoelastic model to simulate the dynamic behavior (Saenger et al., 2011; Wang et al., 2017). Quintal et al. (2016) use a simple hydromechanical approach to model coupled fluid-solid interaction (FSI) at the pore scale. In their work, they solve the quasistatic, linearized Navier-Stokes' equation for laminar flow of a Newtonian fluid in the pore space and the elasticity equation for solid grain. They apply their method to a 2D geometry and compare their results with those obtained by solving Biot's equations of poroelasticity (Quintal et al., 2011, 2014).

The goal of the work presented here was to numerically simulate a fully coupled FSI at the pore scale for digital rock samples. We used the finite-element method to model the solid grains as elastic material using Hooke's law and the pore fluids as Newtonian fluids using the Navier-Stokes' equation with appropriate coupling between the solid and liquid phases, accounting for inertial effects in the solid and the fluid. In cases in which the effective medium theory (EMT) limits were valid (wavelengths longer than the scale of sample heterogeneities), we calculated the P-wave modulus M and attenuation Q^{-1} as a function of frequency. We also used viscoelasticity theory to calculate the dynamic P-wave phase velocity V_P using M and the Q^{-1} results. The remainder of this paper details these efforts and is organized as follows. First, we describe the setup of the numerical experiment. The physics and the boundary conditions that were used to set up the numerical scheme are explained. We also describe the coupling process between the solid and fluid that helps to model the FSI. Second, we discuss our application of

this method to a 2D case with a set of connected cracks. We use the numerical solutions to calculate and analyze the pressure differences in the pore space at different frequencies. We compared the results from this case with the results obtained by performing a static numerical experiment considering the fluid as an elastic material. Third, we present a method for estimation of M and Q^{-1} from the simulation results, and we use the estimated values to calculate V_P dispersion curve at the EMT limit. Fourth, we present a parametric study that sheds light on the effects of the pore aspect ratio and viscosity of the fluid on the simulation results. Finally, we discuss our application of the method to a 3D digital rock sample of Berea sandstone in which the pressure in the pore space was calculated at different frequencies.
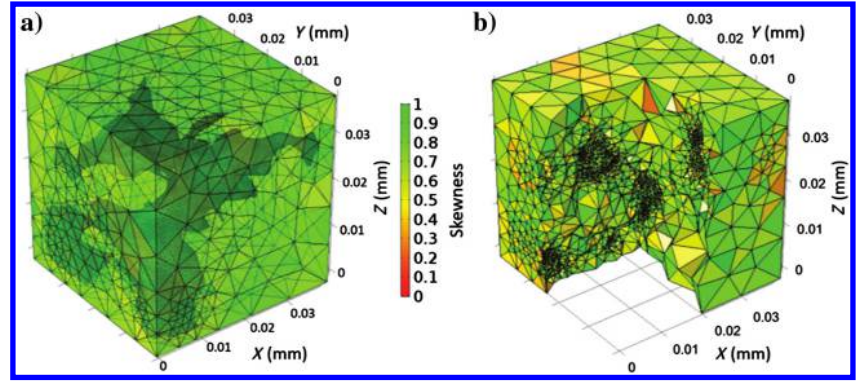

Figure 3. (a) Unstructured tetrahedral mesh for the 3D Berea geometry with skewness of the mesh elements representing the mesh quality shown in color. (b) Inside view of the mesh showing that the grain is meshed with coarse elements and the pore space is meshed with finer elements. The meshing at the interface between the solid and pore is shown in this view.

NUMERICAL SETUP

In this work, we considered the grain as an elastic material and the pore fluid as a compressible Newtonian fluid with density varying as a function of pressure derived using the definition of compressibility of a fluid (equation 1):

$$\rho = \rho_0(1 + (P - P_0)/K_f), \quad (1)$$

where ρ is the density of fluid, ρ_0 is the reference density of the fluid at reference pressure of P_0, and K_f is the bulk modulus of fluid. The properties of the material in grain and the pore (Table 1) are kept the same for all of the simulations, except in the parametric study in which the viscosity of the fluid is changed to assess its impact on the dispersion curves.

The equation of motion along with the constitutive relation for the material is solved for the solid grain to compute stresses and strains. We assume a linear isotropic elastic material for the solid part, for which the constitutive relationship is given by Hooke's law (equation 2):

$$\sigma_{ij} = \lambda \delta_{ij} \epsilon_{\alpha\alpha} + 2\mu \epsilon_{ij}, \quad (2)$$

where σ_{ij} and ϵ_{ij} are the elements of the stress and strain tensor, respectively, and λ and μ are the Lame's constants. The equation of motion is given by Newton's second law of motion, which is formulated in the spatial domain using the Cauchy stress tensor σ. We account for the mass effects in the dynamic behavior of the solid by incorporating the inertial terms. The equation of motion is given by $\rho(\partial^2 u/\partial t^2) = \nabla.\sigma = \text{div}\sigma$. For the pore fluid, we compute the pressure and velocity fields by solving the compressible form of the Navier-Stokes' equation (equation 3) for conservation of momentum:

$$-\nabla P + \nabla \cdot (\eta(\nabla v + (\nabla v)^T) - \frac{2}{3}\eta(\nabla \cdot v)I) + F$$
$$= \rho \frac{\partial v}{\partial t} + \rho v \cdot \nabla v, \quad (3)$$

where P is the pore pressure, η is the dynamic viscosity, v is the fluid velocity vector, F is the volume force vector, ∇ is the spatial
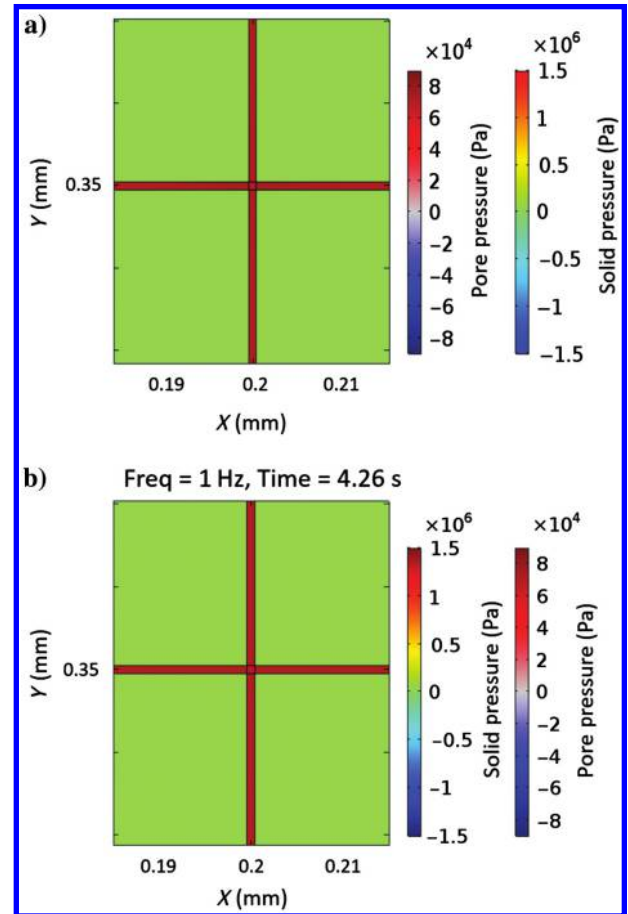

Figure 4. (a) Solid pressure and pore pressure obtained for stationary structural mechanics numerical simulation considering the pore fluid as an elastic material. (b) Solid pressure and pore pressure obtained from low-frequency (1 Hz) coupled FSI numerical simulation at the last time step. The "figures" are not the same; rather, the pressures in both cases are the same, indicating that the FSI solution at low frequency matches the stationary solution considering the fluid as an elastic material.

gradient, ρ is the density, and t is the time. We solve the continuity equation (equation 4) for the conservation of mass:

$$\frac{\partial \rho}{\partial t} + \nabla \cdot (\rho v) = 0, \tag{4}$$

where ∇ is the spatial gradient, ρ is the density, t is the time, and v is the velocity.

The boundary conditions for the numerical experiment are set to simulate a P-wave modulus experiment as follows. The bottom face of the model is fixed with zero displacement; the side faces have a

roller boundary condition, in which the displacement normal to the face is zero. The top boundary is assigned a sinusoidal displacement u normal to the face as a function of frequency f (equation 5):

$$u = 10^{-9} * \sin(2\pi t f), \tag{5}$$

where u is the displacement, t is the time, and f is the frequency. In total, five cycles of the displacement are applied in each case for the numerical solution to reach a steady state. The fifth cycle is extended such that the last time corresponds to the maximum displacement. In this work, we only consider the undrained pore volume. Hence, a no-flux boundary condition is used for the fluid. The two-way coupling between the solid grain and the pore fluid is done using an arbitrary Lagrangian-Eulerian method (Donea, 1982) to combine the fluid flow that is formulated in the Eulerian domain (spatial frame), and the solid mechanics formulated in the Lagrangian domain (material frame). The solid displacement is coupled to the fluid velocity at the interface between the two domains (equation 6):

$$v_{\text{wall}} = \frac{du_{\text{solid}}}{dt}, \tag{6}$$

where t is the time, v_{wall} is the velocity of the wall, and u_{solid} is the displacement of solid at the interface between the solid and fluid domains. The initial values of structural displacement for the solid grain are zero. The initial values of pore fluid velocity and pressure are zero. The reference pressure and temperature for the Navier Stokes' equation in the pore fluid are taken as 1 atm and 273 K, respectively. We perform a 2D plain strain approximation for 2D geometry in which all out-of-plane strain components of the total strain are zero.

We considered two geometries in this work. The first is a 2D section with two connected cracks and referred to in this paper as 2D connected crack geometry. The connected crack geometry has two planar rectangular cracks with a crack length of 0.3 mm, crack width of 0.001 mm, and an aspect ratio of 1:300 for each crack. We also performed a parametric study by numerically simulating two other cases: one by changing the crack length to 0.1 mm and another by changing the crack width to 0.01 mm. In these two cases, the crack aspect ratios are 1:100 and 1:30, respectively. Unless otherwise specified, the 2D connected crack geometry refers to the case with a crack aspect ratio of 1:300. The pore space is enclosed by a 0.4×0.6 mm rectangle that forms the solid grain (Figure 1a). The porosity of the 2D connected crack geometry is approximately 0.25%. This simple 2D geometry (based on Quintal et al., 2016) is used to understand the physics and establish the numerical setup before being simulated on a complex geometry. The crack orientations are arranged such that, based on the applied vertical displace-
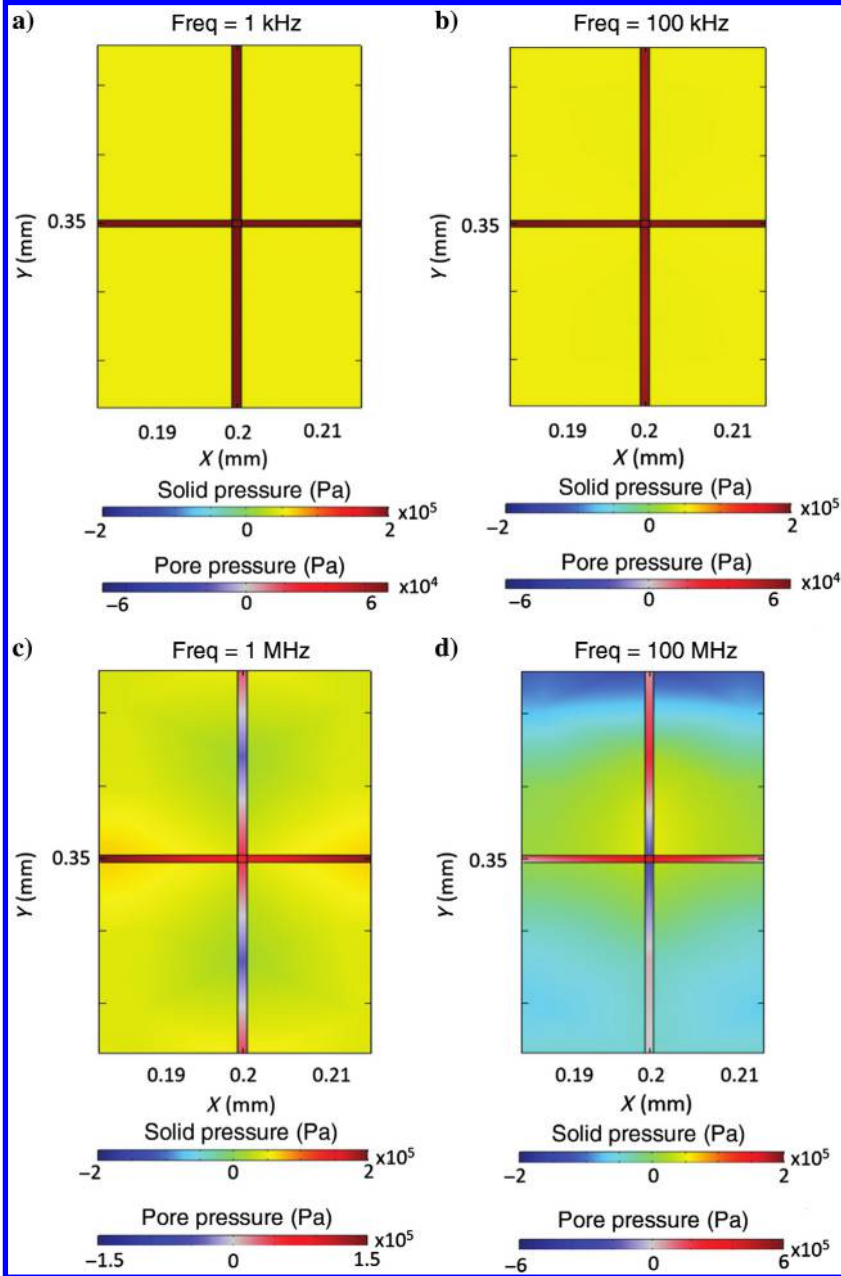

Figure 5. Solid pressure and pore pressure at the last time step obtained from coupled FSI numerical simulations at frequencies of (a) 1 kHz, (b) 100 kHz, (c) 1 MHz, and (d) 100 MHz. The high and low values are represented by warm and cool colors, respectively. Pore pressure heterogeneities can be observed at higher frequencies.

ment, one of the cracks is more compliant than the other. This geometry helps to induce a pore-pressure difference between the two cracks. The second geometry is a 3D micro-CT scan of a Berea sandstone of dimensions $0.36 \times 0.36 \times 0.36$ mm (Figure 2) and is referred to here as Berea geometry. The porosity of the sample is approximately 10%. The whole sample is enclosed in a cube of $0.4 \times 0.4 \times 0.4$ mm that helps in the application of the boundary conditions for the numerical calculation. Each of these geometries is discretized using an unstructured mesh with mostly tetrahedral elements. We used rectangular elements for the pore space in the connected cracks geometry with five elements covering the width of the pore space to resolve the geometry. In general, the mesh has finer elements in the pore space than the grain to capture the microstructure. The mesh for the 2D connected crack geometry (Figure 1b and 1c) has approximately 8000 elements, and the mesh for the Berea geometry (Figure 3) has approximately 327,000 elements.

The total number of degrees of freedom solved in the 2D connected cracks geometry is approximately 33,500, whereas the total number of degrees of freedom in the Berea geometry is approximately 1,245,000. A quadratic Lagrange shape function is used for the solid displacement, and P1 (linear) shape functions are used for the fluid velocity field and pressure. We used the COMSOL Multiphysics finite-element solver to solve the time-dependent initial-boundary value problem. Coupled FSI problems can be solved numerically using a fully coupled direct solver approach or using an iterative solver. Direct solvers are more robust but require more memory. For the 2D problem, we used a time-dependent fully coupled solver (commonly known as the monolithic approach). A direct PARDISO solver (Petra et al., 2014) is used for solving the linear equations for the 2D connected cracks geometry case. An iterative geometric multigrid solver (Briggs, 2000) is used to solve the linear equations for the Berea geometry case as the number of degrees of freedom in this case is very large, limiting the use of a direct solver. The convergence criteria for both cases are based on the relative tolerance or error in the integration step. A lower value of the relative tolerance will ensure more accuracy in the solution, but it will also increase the computation time. Here, we used a relative tolerance value of 0.01 for the 2D cases and 0.1 for the 3D cases. The computations were done on a Dell Workstation Precision T7600 with an Intel Xeon 3.1 GHz (32 CPUs) processor and 128 GB RAM. The computation time for the 2D geometry for each frequency is approximately 2 min, and for the 3D geometry it is approximately 40 min. We performed EMT approximations to calculate the effective M, Q^{-1},

and V_P at frequencies at which the approximations are valid. Details of the calculations used in our work are described in Appendix A.
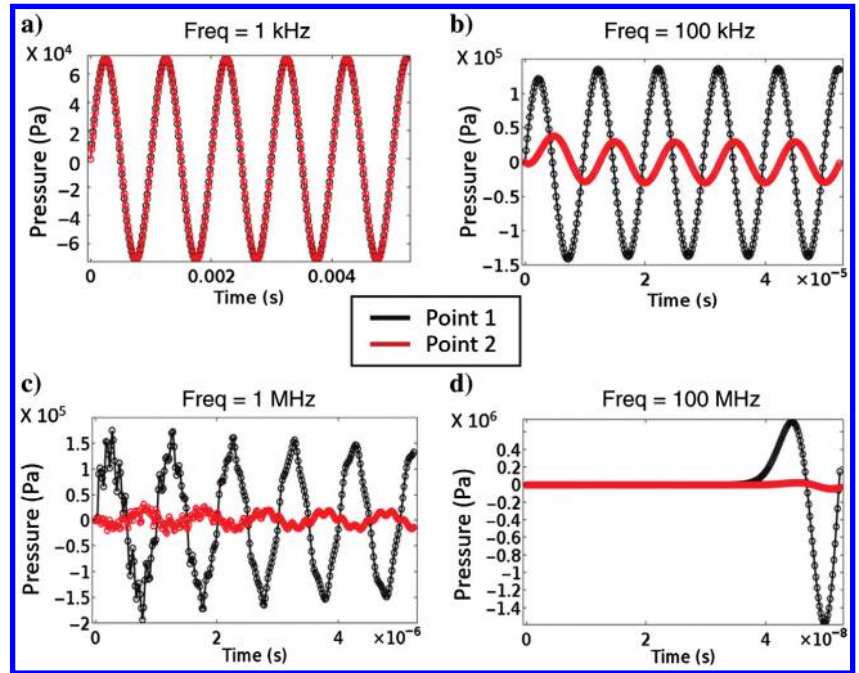

Figure 6. Pore pressure as a function of time for the points — points 1 and 2 for 2D connected cracks geometry obtained from the coupled FSI numerical simulations at frequencies of (a) 1 kHz, (b) 100 kHz, (c) 1 MHz, and (d) 100 MHz.
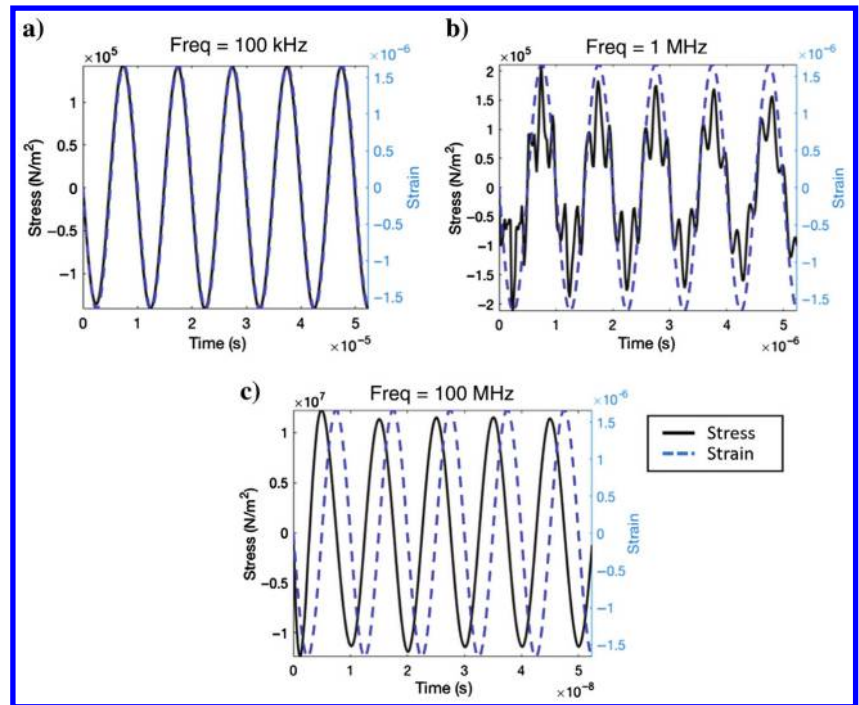

Figure 7. Average stress versus average strain at the top boundary of the 2D connected cracks' geometry obtained from FSI numerical simulations at frequencies of (a) 100 kHz, (b) 1 MHz, and (c) 100 MHz. The average stress and strain reach a steady state solution at the end of the displacement cycle at frequencies corresponding to the EMT limits. At 100 MHz frequency, the average stress and strain do not have a steady state solution.

RESULTS

2D connected cracks geometry

We first performed the numerical simulation on the 2D connected cracks geometry for the low-frequency case by applying a boundary
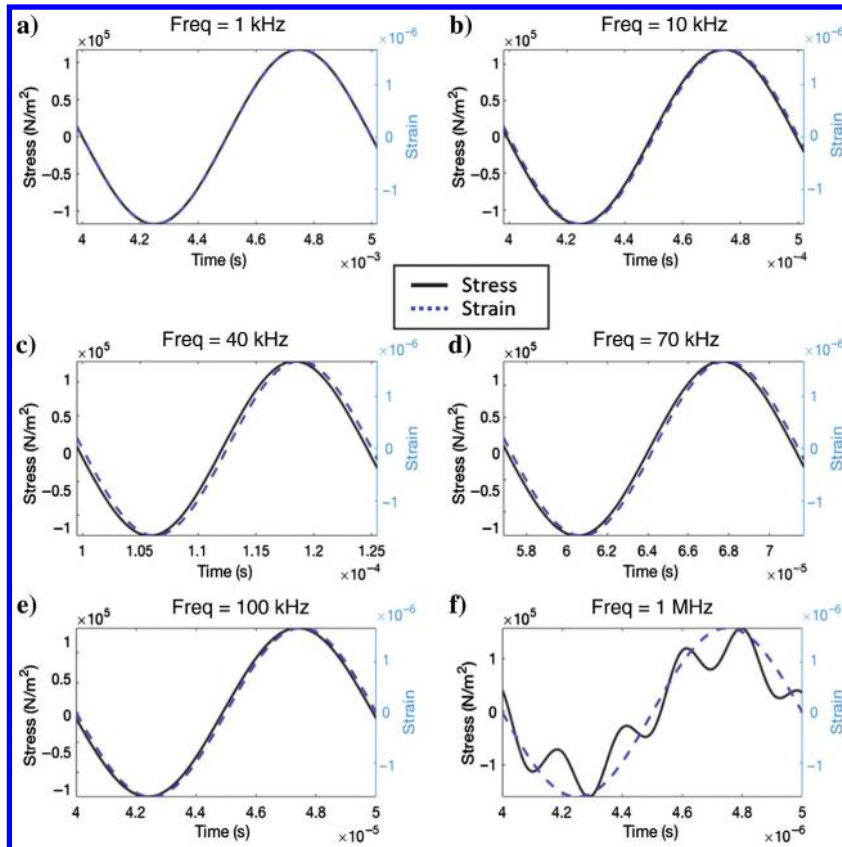

Figure 8. One cycle of average stress versus average strain at the top boundary of the 2D connected cracks' geometry obtained from FSI numerical simulations at frequencies of (a) 1 kHz, (b) 10 kHz, (c) 40 kHz, (d) 70 kHz, (e) 100 kHz, and (f) 1 MHz.
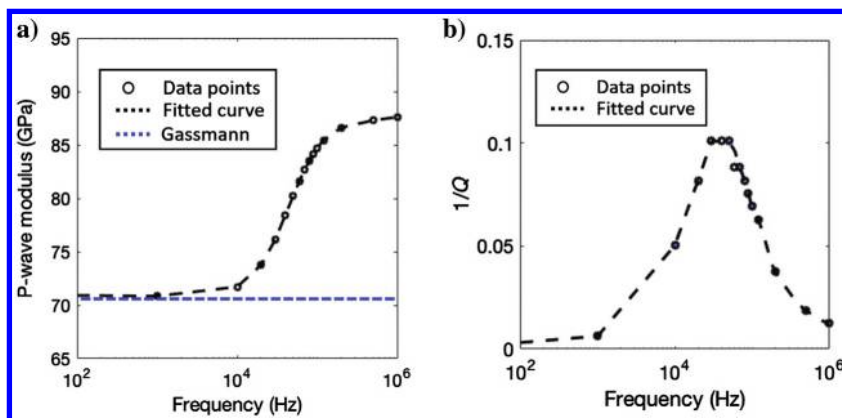

Figure 9. (a) Effective P-wave modulus versus frequency obtained from results of FSI-based numerical simulations using EMT. The effective P-wave modulus obtained using numerical simulation considering fluid as an elastic material is also overlaid. This P-wave modulus corresponds to the lower limit or one obtained using Gassmann's approximations. (b) Effective attenuation (Q^{-1}) versus frequency obtained from results of FSI-based numerical simulations using EMT.

displacement at a frequency of 1 Hz. The pressure in this case is expected to be homogeneous and to follow the assumptions mentioned in Gassmann (1951). We compare the pore pressure in this low-frequency case with the numerical simulation in which the pore fluid is considered an elastic material with elastic properties comparable to the pore fluid mentioned in Table 1. The pressure (at the last time step) in the solid grain and the pore fluid (Figure 4a) is comparable to the pressure obtained from the solid mechanics simulation (Figure 4b). This helps in establishing our numerical scheme. Numerical simulations that approximate the pore fluid as an elastic material cannot handle dynamic effects due to the pore fluid flow; hence, the pore pressure is always homogeneous, approximating very low-frequency conditions. The elastic moduli calculations using these simulations correspond to the Biot-Gassmann low-frequency limit. Second, we carried out the simulations for a sweep of frequencies ranging from 1 Hz to 100 MHz — that spans the effective medium and the non-effective medium frequencies for this 2D geometry. The pore pressure and the pressure in the solid for some of the frequencies (1 kHz, 100 kHz, 1 MHz, and 100 MHz) are shown in Figure 5a–5d. The pore pressures at the two points, point 1 corresponding to the horizontal crack oriented toward the maximum normal stress given the boundary conditions and point 2 corresponding to the vertical crack oriented away from the maximum normal stress given the boundary conditions (Figure 1) are shown for different frequencies (1 kHz, 100 kHz, 1 MHz, and 100 MHz) in Figure 6a–6d. The pore pressure at these two points is in equilibrium at lower frequencies in the kHz range (Figure 6a) because the fluid gets ample time to flow from the high-pressure zones in the compliant horizontal crack to the low-pressure zones in the vertical crack. At higher frequencies of the order of MHz, we observe that the pore pressures at points 1 and 2 are no longer in equilibrium (Figure 6b and 6c). At these higher frequencies, the pore fluid does not have enough time to move from the high-pressure to the low-pressure areas in the cracks. At very high frequencies of the order of 100 MHz, the wavelength of the displacement applied at the top is comparable to or less than the size of the sample. As a result, we can observe wave propagation in the sample and scattering effects that lead to large pore pressure heterogeneities (Figure 6d). The EMT calculations are not applicable at such large frequencies. The average stresses and strains at the top boundary of the sample calculated from the simulation results for different frequencies (Figure 7a–7c) show that the average stress and strain reach a steady state for all frequencies except when the frequency is very high (Figure 7c). At this high frequency, scattering and resonance effects predominate and the EMT

approximations are invalid. The phase differences between one cycle of the average stress and average strain for some of the frequencies (1 kHz, 10 kHz, 40 kHz, 70 kHz, 100 kHz, and 1 MHz) corresponding to the EMT approximations are shown in Figure 8a–8f. At a frequency of 1 kHz, the average stress and strain are in phase (Figure 8a). However, as we increase the frequency, we observe that the phase difference between the average stress and strain first increases and then starts to decrease (Figure 8b–8e). At a high frequency of 1 MHz, we start observing scattering effects in the average stress and strain (Figure 8f). The average stress and strain were used to calculate the M, Q^{-1}, and V_P for the frequencies in which EMT approximations are valid using the method described in Appendix A. The real part of M, also known as storage modulus (Figure 9a), shows the maximum dispersion at approximately 50 kHz, which corresponds to the Debye peak in the calculated Q^{-1} curve (Figure 9b). The calcu-

lated V_P (Figure 10) also shows the dispersion with the lower limit at approximately 5200 m/s, which matches the value obtained using Gassmann's approximation and the higher limit at approximately 5800 m/s. Similar calculations were made by changing the viscosity of the pore fluid by orders of magnitude. The normalized V_P for different pore-fluid viscosities (Figure 11) shows that the dispersion curve shifts toward lower frequencies as the viscosity of the pore fluid is increased. As a result, for viscous fluid, e.g., heavy oils, we can expect the dispersion effects at lower frequencies in contrast to rocks saturated with water or gas. We also carried out a parametric study by changing the aspect ratio of the cracks forming the pore space. The normalized V_P calculated for different aspect ratios (Figure 12) show that the dispersion curves move toward the lower frequencies as the aspect ratio of the microcracks is decreased. Based on this result, we can conclude that microcracks that are difficult to image and resolve in the digital rock samples when saturated with fluids can have significant dispersion effects at lower frequencies.
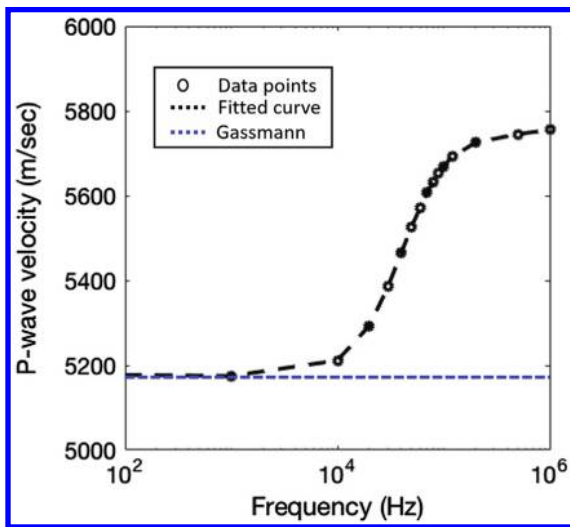
Berea sandstone

The numerical method established using the 2D-connected-crack geometry was applied on a 3D digital rock sample of Berea sandstone. The simulations were done for a sweep of frequencies ranging from 10 Hz to 100 MHz, which spans the effective medium and the noneffective medium frequencies for this 3D sample. The pore pressure at the last time step is shown for some of the frequencies (1 kHz, 100 kHz, 10 MHz, and 100 MHz) in Figure 13a–13d. The fluid velocity fields for the unrelaxed state at frequencies of 10 and 100 MHz are also represented by the black arrows in Figure 13c and 13d. The pore pressure at the points 1 and 2 shown in Figure 2 is plotted for various frequencies (1 kHz, 100 kHz, 10 MHz, and 100 MHz) in Figure 14a–14d. The coefficient of variation of pore pressure at the last time step is plotted as a function of frequency in Figure 15. Our results show that at low frequencies, the pore pressure is homogeneous throughout the pore space. However, the pore pressure at high frequency is heterogeneous. This pressure heterogeneity leads to the local fluid flow, in which the fluid starts to flow from the high-pressure areas to areas of low pressure in the pore space. The calculations for effective medium M, Q^{-1}, and V_P were also carried out for frequencies in which the EMT approximations were valid. Note that the Berea sample used in our simulations is

Figure 10. Effective P-wave phase velocity versus frequency obtained from the effective P-wave modulus and the attenuation (Q^{-1}) values. The effective P-wave phase velocity corresponding to Gassmann's approximation obtained using the numerical simulation considering the fluid as an elastic material is overlaid.
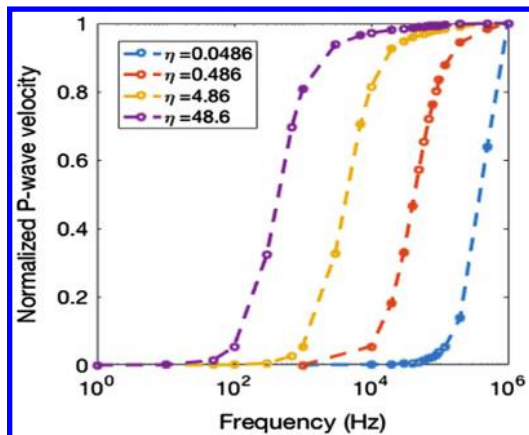

Figure 11. Normalized P-wave phase velocity versus frequency for fluids with different viscosities (in Pa-s) obtained using FSI-based numerical simulations. The dispersion curves shift to lower frequencies with the increase in fluid viscosity.
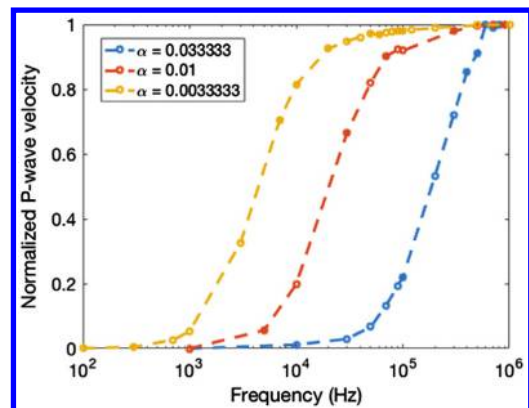

Figure 12. Normalized P-wave phase velocity versus frequency for pores with different aspect ratios obtained using FSI-based numerical simulations. The dispersion curves shift to lower frequencies with the decrease in the aspect ratio of the microcracks.

small in dimension and may not be a representative elementary volume. We found that the lower and upper limits of the V_P dispersion curve are approximately the same, given the microstructure and the material properties. The upper and lower limits of the real part of M calculated using the average stress and strain at the top boundary are approximately 77 GPa and did not show significant dispersion.

DISCUSSION

We established a numerical method to conduct multiphysics FSI simulation for digital rock samples, and captured the physics related to FSI at the pore scale, including solid and fluid inertial effects. The method provides greater insights into the dynamic effects of the presence of pore fluid at different frequencies. At low frequencies (10 Hz), the pore fluid is in equilibrium and the pore pressure is homogeneous. At higher frequencies (100 kHz), pore-pressure

heterogeneities were observed. At very high frequencies (100 MHz) in which the wavelength of the applied displacement is smaller (approximately 1/100th) than the size of the sample, we observed wave propagation and scattering effects in the solid and the pore fluid. Thus, we can conclude that the pore fluid effects become prominent at the higher frequencies and that the dynamic effects of the fluid in digital rock samples can only be studied by considering the coupled simulation approach. We also calculated the effective M, Q^{-1}, and V_P using EMT approximations. A Debye peak in the Q^{-1} curve for the 2D connected cracks geometry occurred at approximately 50 kHz. Our parametric studies showed that the V_P dispersion curves shift to lower frequencies as we increase the fluid viscosity or decrease the aspect ratio of the microcracks. This behavior is consistent with theoretical rock-physics models. We also used the proposed numerical method to simulate coupled FSI in a digital rock sample of Berea sandstone. Our observations for the 3D Berea sandstone are consistent with the observations from the 2D connected cracks geometry. The pore pressure was in equilibrium for the low frequencies (1 kHz). As we increased the frequency (10 MHz), the pore pressure was no longer homogeneous. At higher frequencies (100 MHz), scattering effects and higher pore pressure heterogeneities were observed. Our EMT calculations showed that given the microstructure of the 3D Berea sample, we do not have significant dispersion in M or V_P. However, the 2D connected cracks geometry demonstrates that microcracks that are below imaging resolution can play a major role in dispersion. Hence, the dispersion from the microcracks in the 3D Berea sample may not be observed due to the limitations in image resolution.

A critical aspect in numerical methods is the selection of appropriate mesh size and time step size. For the 2D geometry, we ensured that the thinnest part of the geometry (rectangular cracks) was resolved by covering the width using five rectangular elements. A numerical analysis on the average solid and pore pressure at the last time step for low frequency (1 kHz) and high frequency (100 MHz) using a coarser mesh (approximately 274,000 elements) and finer mesh (approximately 368,000 elements) as compared to the mesh used in this study (approximately 327,000 elements) showed that the solution is stable with the mesh used in this study (Figure 16). The time step was selected such that each cycle of the applied sinusoidal displacement consists of 20 samples to ensure numerical stability of the solution.

The results from our proposed numerical method increase our understanding of the stress heterogeneity and the pore pressure differences in the digital rock samples. These results can only be obtained using coupled FSI numerical experiments and cannot be obtained from standard laboratory experiments. We found that, at lower frequencies in which the EMT approxima-
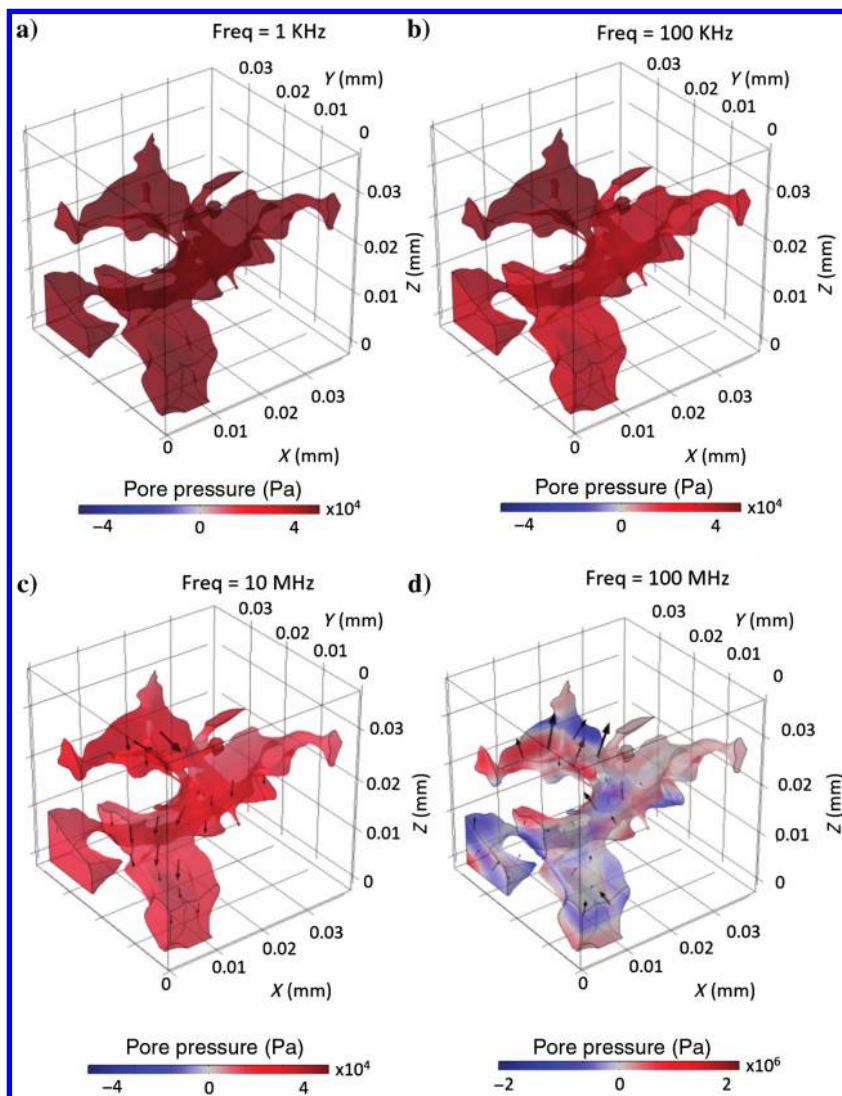

Figure 13. Pore pressure for 3D Berea digital rock sample at the last time obtained using FSI-based numerical simulations at frequencies — (a) 1 kHz, (b) 100 kHz, (c) 10 MHz, and (d) 100 MHz. The high and low values are represented by hot and cool colors, respectively. The velocity field at the last time for frequencies (c) 10 MHz and (d) 100 MHz corresponding to unrelaxed state is plotted with the black arrows.

tions are valid, the results obtained by considering the mass effects in the solid are the same as results obtained without considering the mass effects in the solid. However, at higher frequencies, the stresses in the solid can be correctly calculated only by considering the inertial effects. Apart from the stress and pore pressure distributions, we can also obtain dispersion curves for digital rock samples using the method developed in this study. The dispersion curves will be useful to understand the differences between seismic measurements taken at different frequencies — surface seismic (low frequency), borehole seismic (100 kHz), and laboratory measurements (MHz). The results give us a better estimation of effective elastic properties of the rock and the fluid and allow us to develop reliable rock-physics models that can be used for reservoir characterization workflows.

CONCLUSION

Dynamic fluid effects in the rocks play an important role in velocity dispersion and attenuation at different frequencies. Numerical simulations that account for coupled FSI help us to analyze and understand these effects. Stress and pore pressure heterogeneities can be obtained using the proposed numerical method. These results can provide insights into better effective medium models and can be useful for engineering purposes such as enhanced oil recovery.

ACKNOWLEDGMENTS

DATA AND MATERIALS AVAILABILITY

Data associated with this research are available and can be obtained by contacting the corresponding author.
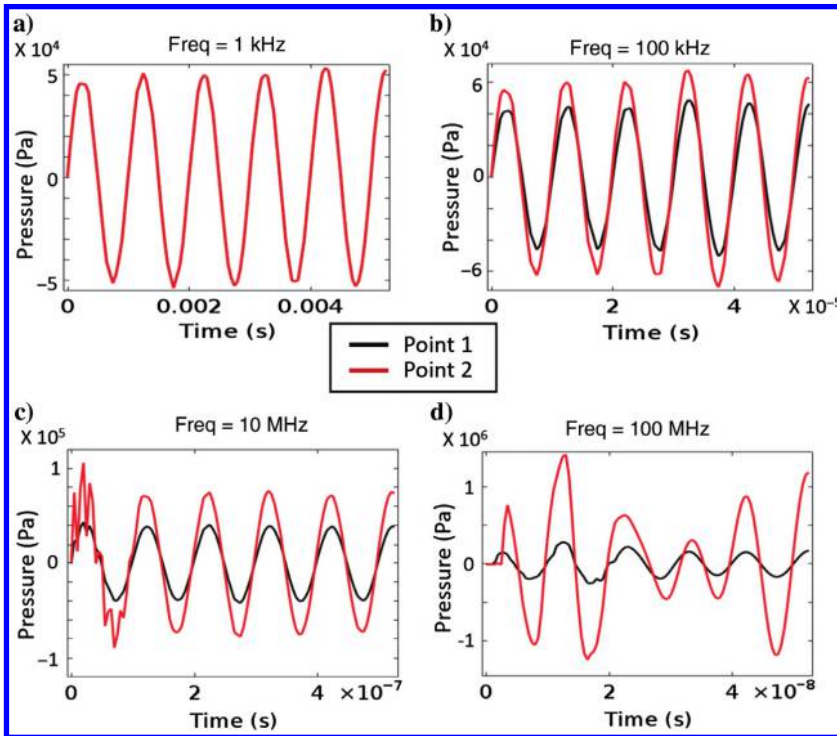

Figure 14. Pore pressure as a function of time for points — points 1 and 2 for 3D Berea obtained from the coupled FSI numerical simulations at frequencies — (a) 1 kHz, (b) 100 kHz, (c) 10 MHz, and (d) 100 MHz.
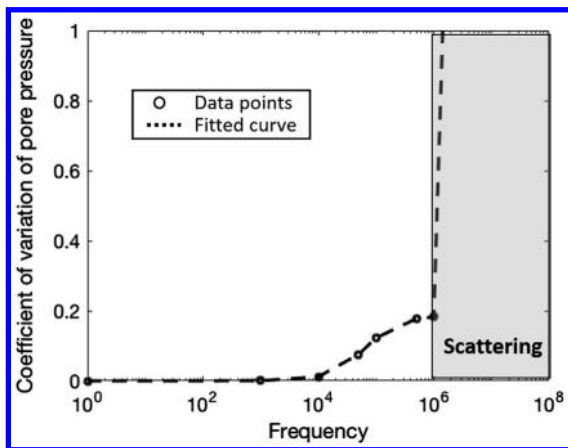

Figure 15. Coefficient of variation of pore pressure at last time step for 3D Berea obtained from the coupled FSI simulations is plotted as a function of frequency. The low frequencies at which the pore pressure is equilibrated has a zero coefficient of variation. The coefficient of variation is highest for the scattering domain.
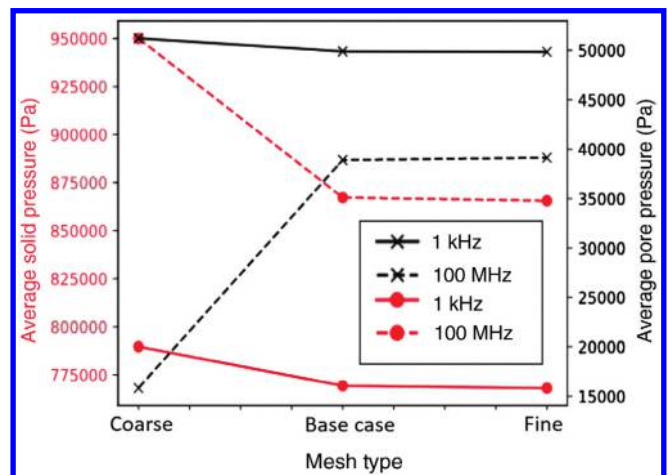

Figure 16. Average solid pressure and average pore pressure at the last time step for low frequency (1 kHz) and high frequency (100 MHz) for the 3D Berea geometry showing the base case, and the fine mesh has similar results.

APPENDIX A

EFFECTIVE P-WAVE MODULUS M, ATTENUATION q^{-1}, AND VELOCITY V_P CALCULATIONS

Scale of heterogeneity (d) and the dominant wavelength (λ) determine the regime in which EMT approximations are valid in elastic and viscoelastic media (Marion et al., 1994; Das et al., 2019). Although EMT approximations might be valid for $\lambda/d \geq 10$, here we assume EMT approximations for values of $\lambda/d \geq 100$ to avoid any transition zone from the ray theory to EMT. In the EMT domain, calculations are done by taking an average of stress and displacement at the top boundary of the sample. The effective modulus of the composite is calculated by taking the ratio of the average stress and strain at the top surface. In the 2D cases, we calculate the average stress and strain in the y-direction. Strain in the y-direction is calculated by dividing the average displacement by the length of the sample in the y-direction. In the 3D cases, we perform similar calculations in the z-direction. Because the applied displacement boundary condition at the top surface is given by a sinusoidal function of time (equation 5), the average stresses and strains at the top boundary calculated from the simulation results are also sinusoidal functions having the same frequency as the applied displacement. However, at higher frequencies, in which the fluid pressures are not equilibrated, the average stresses and strains at the top boundary will be out of phase. In the EMT limit, we can assume the composite as an effective viscoelastic material. The average stress and average strain can be expressed using theories of viscoelasticity (Lakes, 2009) using equations A-1 and A-2, respectively:

$$\sigma(t) = \sigma_0 \sin(2\pi f t), \tag{A-1}$$

$$\epsilon = \epsilon_0 \, \sin(2\pi f t + \phi), \tag{A-2}$$

where σ is the stress, σ_0 is the stress amplitude, ϵ is the strain, ϵ_0 is the strain amplitude, f is the frequency, t is the time, and ϕ is the phase difference between stress and strain. The phase difference φ between the stress and strain can also be expressed in terms of time lag (equation A-3):

$$\phi = 2\pi f t_0, \tag{A-3}$$

where t_0 is the time lag between stress and strain that can be calculated as the difference between the time at which the stress and strain amplitudes are maximum. To calculate the frequency dependent M, Q^{-1}, and V_P, we take the Fourier transform of the time-dependent stress (equation A-1) and strain (equation A-2). The frequency-domain stress and strain are given in equations A-4 and A-5, respectively:

$$\sigma(\omega) = \sqrt{\frac{\pi}{2}}\sigma_0 i[\delta(\omega - 2\pi f) - \delta(\omega + 2\pi f)], \tag{A-4}$$

$$\epsilon(\omega) = \sqrt{\frac{\pi}{2}}\epsilon_0 i[e^{-2\pi i \nu t_0}\delta(\omega - 2\pi f) - e^{-2\pi i \nu t_0}\delta(\omega + 2\pi f)], \tag{A-5}$$

where δ is the Kronecker delta function and ω is the angular frequency. Because the applied displacement is monochromatic, the stress and strain at that frequency is given in equation A-6 and A-7, respectively:

$$\sigma(2\pi f) = \sigma_0 i\sqrt{\frac{\pi}{2}}, \tag{A-6}$$

$$\epsilon(2\pi f) = \epsilon_0 i\sqrt{\frac{\pi}{2}}[e^{-2\pi i f t_0}]. \tag{A-7}$$

The complex P-wave modulus M at frequency f can be calculated using the stress and strain at frequency f and is given in equation A-8:

$$\begin{aligned} M(f) &= \frac{\sigma_0}{\epsilon_0[e^{-2\pi i f t_0}]} \\ &= \frac{\sigma_0}{\epsilon_0[\cos(2\pi f t_0) - i \, \sin(2\pi f t_0)]}. \end{aligned} \tag{A-8}$$

Upon simplification, the real part of M, also known as the storage moduli, is given in equation A-9, and the imaginary part of M, also known as the loss moduli, is given in equation A-10:

$$\text{Re}(M) = \frac{\sigma_0}{\epsilon_0}\cos(2\pi f t_0) \quad = \frac{\sigma(t_1)}{\epsilon(t_1)}, \tag{A-9}$$

where t_1 is the time at which the strain has maximum amplitude

$$\text{Im}(M) = \frac{\sigma_0}{\epsilon_0}\sin(2\pi f t_0). \tag{A-10}$$

The term Q^{-1} can be calculated by taking the ratio of the $\text{Im}(M)$ and $\text{Re}(M)$ (equation A-11):

$$Q^{-1} = \frac{\sin(2\pi f t_0)}{\cos(2\pi f t_0)} \quad = \tan(\phi). \tag{A-11}$$

The term V_P can then be calculated using equation A-12:

$$v = v_0 \left(\frac{2(1 + (Q^{-1})^2)}{\sqrt{1 + (Q^{-1})^2} + 1}\right)^{1/2}. \tag{A-12}$$

REFERENCES

Andrä, H., N. Combaret, J. Dvorkin, E. Glatt, J. Han, M. Kabel, Y. Keehm, F. Krzkilla, M. Lee, C. Madonna, M. Marsh, T. Mukerji, E. H. Saenger, R. Sain, N. Saxena, S. Ricker, A. Wiegmann, and X. Zhan, 2013a, Digital rock physics benchmarks — Part 1: Imaging and segmentation: Computers and Geosciences, **50**, 25–32, doi: 10.1016/j.cageo.2012.09.005.

Andrä, H., N. Combaret, J. Dvorkin, E. Glatt, J. Han, M. Kabel, Y. Keehm, F. Krzkilla, M. Lee, C. Madonna, M. Marsh, T. Mukerji, E. H. Saenger, R. Sain, N. Saxena, D. Ricker, A. Wiegmann, and X. Zhan, 2013b, Digital rock physics benchmarks — Part 2: Computing effective properties: Computers and Geosciences, **50**, 33–43, doi: 10.1016/j.cageo.2012.09.008.

Arns, C. H., F. Bauget, A. Limaye, A. Sakellariou, T. J. Senden, A. P. Sheppard, R. M. Sok, W. V. Pinczewski, S. Bakke, L. I. Berge, P. E. Oren, and M. A. Knackstedt, 2005, Pore scale characterization of carbonates using X-ray microtomography: SPE Journal, **10**, 475–484.

Arns, C. H., M. A. Knackstedt, W. V. Pinczewski, and E. G. Garboczi, 2002, Computation of linear elastic properties from microtomographic images:

Methodology and agreement between theory and experiment: Geophysics, **67**, 1396–1405, doi: 10.1190/1.1512785.

Arns, C. H., M. A. Knackstedt, W. V. Pinczewski, and W. B. Lindquist, 2001, Accurate estimation of transport properties from microtomographic images: Geophysical Research Letters, **28**, 3361–3364, doi: 10.1029/2001GL012987.

Briggs, W. L., 2000, A multigrid tutorial: SIAM.

Chapman, M., S. V. Zatsepin, and S. Crampin, 2002, Derivation of a microstructural poroelastic model: Geophysical Journal International, **151**, 427–451, doi: 10.1046/j.1365-246X.2002.01769.x.

Das, V., T. Mukerji, and G. Mavko, 2019, Scale effects on velocity dispersion and attenuation (Q^{-1}) in layered viscoelastic medium: Geophysics, **84**, no. 3, 1–98, doi: 10.1190/geo2018-0154.1.

Donea, J., 1982, An arbitrary Lagrangian-Eulerian finite element method for transient dynamic fluid-structure interaction: Computer Methods in Applied Mechanics and Engineering, **33**, 689–723, doi: 10.1016/0045-7825(82)90128-1.

Dvorkin, J., N. Derzhi, E. Diaz, and Q. Fang, 2011, Relevance of computational rock physics: Geophysics, **76**, no. 5, E141–E153, doi: 10.1190/geo2010-0352.1.

Fredrich, J., K. Greaves, and J. Martin, 1993, Pore geometry and transport properties of Fontainebleau sandstone: International Journal of Rock Mechanics and Mining Sciences and Geomechanics, **30**, 691–697, doi: 10.1016/0148-9062(93)90007-Z.

Garboczi, E. J., 1998, Finite element and finite difference programs for computing the linear electric and elastic properties of digital image of random materials: National Institute of Standards and Technology Interagency Report 6269.

Gassmann, F., 1951, Über die Elastizität poröser Medien: Mitteilungen Inst. Geophysik (Zurich) 17, 1–23. Translated and reprinted as: On elasticity of porous media, in M. A. Pelissier, ed., Classics of elastic wave theory: SEG, 2007.

Golab, A., M. A. Knackstedt, H. Averdunk, T. Senden, A. R. Butcher, and P. Jaime, 2010, 3D porosity and mineralogy characterization in tight gas sandstones: The Leading Edge, **29**, 1476–1483, doi: 10.1190/1.3525363.

Gurevich, B., D. Makarynska, O. B. de Paula, and M. Pervukhina, 2010, A simple model for squirt-flow dispersion and attenuation in fluid-saturated granular rocks: Geophysics, **75**, no. 6, N109–N120, doi: 10.1190/1.3509782.

Keehm, Y., T. Mukerji, and A. Nur, 2001, Computational rock physics at the pore scale: Transport properties and diagenesis in realistic pore geometries: The Leading Edge, **20**, 180–183, doi: 10.1190/1.1438904.

Lakes, R., 2009, Viscoelastic materials: Cambridge University Press.

Madonna, C., B. S. G. Almqvist, and E. H. Saenger, 2012, Digital rock physics: Numerical prediction of pressure-dependent ultrasonic velocities using micro-CT imaging: Geophysical Journal International, **189**, 1475–1482, doi: 10.1111/j.1365-246X.2012.05437.x.

Marion, D., T. Mukerji, and G. Mavko, 1994, Scale effects on velocity dispersion: From ray to effective-medium theories in stratified media: Geophysics, **59**, 1613–1619, doi: 10.1190/1.1443550.

Masson, Y. J., and S. R. Pride, 2007, Poroelastic finite-difference modeling of seismic attenuation and dispersion due to mesoscopic-scale heterogeneity: Journal of Geophysical Research, **112**, B03204, doi: 10.1029/2006JB004592.

Mavko, G., and D. Jizba, 1991, Estimating grain-scale fluid effects on velocity dispersion in rocks: Geophysics, **56**, 1940–1949, doi: 10.1190/1.1443005.

Mavko, G., T. Mukerji, and J. Dvorkin, 2009, The rock physics handbook: Tools for seismic analysis in porous media: Cambridge University Press.

Mavko, G., and A. Nur, 1975, Melt squirt in the asthenosphere: Journal of Geophysical Research, **80**, 1444–1448, doi: 10.1029/JB080i011p01444.

Müller, T. M., B. Gurevich, and M. Lebedev, 2010, Seismic wave attenuation and dispersion resulting from wave-induced flow in porous rocks — A review: Geophysics, **75**, no. 5, 75A147–75A164, doi: 10.1190/1.3463417.

Murphy, W. F., K. W. Winkler, and R. L. Kleinberg, 1986, Acoustic relaxation in sedimentary rocks, dependence on grain contacts and fluid saturation: Geophysics, **51**, 757–766, doi: 10.1190/1.1442128.

O'Connell, R. J., and B. Budiansky, 1977, Viscoelastic properties of fluid-saturated cracked solids: Journal of Geophysical Research, **82**, 5719–5735, doi: 10.1029/JB082i036p05719.

Petra, C. G., O. Schenk, M. Lubin, and K. Gärtner, 2014, An augmented incomplete factorization approach for computing the Schur complement in stochastic optimization: SIAM Journal on Scientific Computing, **36**, C139–C162, doi: 10.1137/130908737.

Pinczewski, W. V., and W. B. Lindquist, 2001, Accurate computation of transport properties from microtomographic images: Geophysical Research Letters, **28**, 3361–3364, doi: 10.1029/2001GL012987.

Quintal, B., R. Jänicke, J. G. Rubino, H. Steeb, and K. Holliger, 2014, Sensitivity of S-wave attenuation to the connectivity of fractures in fluid-saturated rocks: Geophysics, **79**, no. 5, WB15–WB24, doi: 10.1190/geo2013-0409.1.

Quintal, B., J. G. Rubino, E. Caspari, and K. Holliger, 2016, A simple hydro-mechanical approach for simulating squirt-type flow: Geophysics, **81**, no. 4, D335–D344, doi: 10.1190/geo2015-0383.1.

Quintal, B., H. Steeb, M. Frehner, and S. M. Schmalholz, 2011, Quasi-static finite-element modeling of seismic attenuation and dispersion due to wave-induced fluid flow in poroelastic media: Journal of Geophysical Research, **116**, B01201, doi: 10.1029/2010JB007475.

Saenger, E. H., F. Enzmann, Y. Keehm, and H. Steeb, 2011, Digital rock physics: Effect of fluid viscosity on effective elastic properties: Journal of Applied Geophysics, **74**, 236–241, doi: 10.1016/j.jappgeo.2011.06.001.

Sain, R., T. Mukerji, and G. Mavko, 2014, How computational rock-physics tools can be used to simulate geologic processes, understand pore-scale heterogeneity, and refine theoretical models: The Leading Edge, **33**, 324–334, doi: 10.1190/tle33030324.1.

Sams, M. S., J. P. Neep, M. H. Worthington, and M. S. King, 1997, The measurement of velocity dispersion and frequency dependent intrinsic attenuation in sedimentary rocks: Geophysics, **62**, 1456–1464, doi: 10.1190/1.1444249.

Saxena, N., R. Hofmann, F. O. Alpak, S. Berg, J. Dietderich, U. Agarwal, K. Tandon, S. Hunter, J. Freeman, and O. B. Wilson, 2017a, References and benchmarks for pore-scale flow simulated using micro-CT images of porous media and digital rocks: Advances in Water Resources, **109**, 211–235, doi: 10.1016/j.advwatres.2017.09.007.

Saxena, N., and G. Mavko, 2016, Estimating elastic moduli of rocks from thin sections: Digital rock study of 3D properties from 2D images: Computers and Geosciences, **88**, 9–21, doi: 10.1016/j.cageo.2015.12.008.

Saxena, N., E. H. Saenger, R. Hofmann, and A. Wiegmann, 2017b, Influence of stress and strain loading conditions on elastic and sonic properties of digital rocks: 87th Annual International Meeting, SEG, Expanded Abstracts, 3882–3887, doi: 10.1190/segam2017-17785203.1.

Tisato, N., and B. Quintal, 2013, Measurements of seismic attenuation and transient fluid pressure in partially saturated Berea sandstone: Evidence of fluid flow on the mesoscopic scale: Geophysical Journal International, **195**, 342–351, doi: 10.1093/gji/ggt259.

Tisato, N., and B. Quintal, 2014, Laboratory measurements of seismic attenuation in sandstone: Strain versus fluid saturation effects: Geophysics, **79**, no. 5, WB9–WB14, doi: 10.1190/geo2013-0419.1.

Wang, Z., D. R. Schmitt, and R. Wang, 2017, Modeling of viscoelastic properties of nonpermeable porous rock saturated with highly viscous fluid at seismic frequencies at the core scale: Journal of Geophysical Research: Solid Earth, **122**, 6067–6086.

Zhan, X., M. S. Lawrence, S. Wave, M. N. Toksöz, and F. D. Morgan, 2010, Pore scale modeling of electrical and fluid transport in Berea sandstone: Geophysics, **75**, no. 5, F135–F142, doi: 10.1190/1.3463704.